Chemical Stability of Zirconolite for Proliferation Resistance under Conditions Typically Required for the Leaching of Highly Refractory Uranium Minerals

Aleksandar N. Nikoloski [1,*], Rorie Gilligan [1], Jonathan Squire [2] and Ewan R. Maddrell [3]

[1] College of Science, Health, Engineering and Education, Murdoch University, Perth 6150, Australia; Rorie.Gilligan@murdoch.edu.au

[2] Sellafield Ltd., Seascale, Cumbria CA20 1PG, UK; jon.squire@sellafieldsites.com

[3] National Nuclear Laboratory, Workington, Cumbria CA14 3YQ, UK; ewan.r.maddrell@nnl.co.uk

[*] Correspondence: A.Nikoloski@murdoch.edu.au; Tel.: +61-8-9360-2835; Fax: +61-8-9360-6343

Abstract: In this study, synthetic zirconolite samples with a target composition $Ca_{0.75}Ce_{0.25}ZrTi_2O_7$, prepared using two different methods, were used to study the stability of zirconolite for nuclear waste immobilisation. Particular focus was on plutonium, with cerium used as a substitute. The testing of destabilisation was conducted under conditions previously applied to other highly refractory uranium minerals that have been considered for safe storage of nuclear waste, brannerite and betafite. Acid (HCl, H_2SO_4) leaching for up to 5 h and alkaline ($NaHCO_3$, Na_2CO_3) leaching for up to 24 h was done to enable comparison with brannerite leached under the same conditions. Ferric ion was added as an oxidant. Under these conditions, the synthetic zirconolite dissolved much slower than brannerite and betafite. While the most intense conditions were observed previously to result in near complete dissolution of brannerite in under 5 h, zirconolite was not observed to undergo significant attack over this timescale. Fine zirconolite dissolved faster than the coarse material, indicating that dissolution rate is related to surface area. This data and the long term stability of zirconolite indicate that it is a good material for long-term sequestration of radioisotopes. Besides its long term durability in the disposal environment, a wasteform for fissile material immobilisation must demonstrate proliferation resistance such that the fissile elements cannot be retrieved by leaching of the wasteform. This study, in conjunction with the previous studies on brannerite and betafite leaching, strongly indicates that the addition of depleted uranium to the wasteform, to avert long term criticality events, is detrimental to proliferation resistance. Given the demonstrated durability of zirconolite, long term criticality risks in the disposal environment seem a remote possibility, which supports its selection, above brannerite or betafite, as the optimal wasteform for the disposition of nuclear waste, including of surplus plutonium.

Keywords: uranium; zirconolite; brannerite; betafite; leaching; kinetics

1. Introduction

Zirconolite, $CaZrTi_2O_7$ is one of several titanate phases present in synthetic titanate ceramics developed for the immobilisation of actinides and fission products in spent nuclear fuel. Other phases include pyrochlore, brannerite and zircon [1].

These minerals frequently contain uranium and/or thorium. In zirconolite, uranium undergoes extensive substitution onto the calcium site [2]. In brannerite, uranium is an essential element while in pyrochlore and zirconolite, actinides and light rare earth elements (REEs) can also take the place of calcium. Synthetic forms of these minerals can substitute other actinides as well, such as plutonium, americium and curium, in the calcium site, being likely too large for the other sites. The

high chemical durability of these materials suggests that they could be ideal for the sequestration of surplus plutonium and other actinides present in spent nuclear fuel. There are reports of zirconolites that have been observed to show evidences of post-crystallization corrosion [3].

Zirconolite has been identified in weathered gravel in Sri Lanka [4], in Western Australian dolerite intrusions [5], in lunar granite [6] and other varied geological settings and/or minero-genetic conditions [7]. Zirconolites up to 650 million years old have been identified in which $^{206}Pb/^{238}U$, $^{207}Pb/^{235}U$ and $^{206}Pb/^{207}Pb$ isotope ratios give consistent ages, indicating that no uranium has been lost from the zirconolite despite the host rock having undergone extensive weathering over the 650 million years since formation [2]. It is also worth noting the existence of 2 billion year old zirconolite from Phalaborwa in South Africa as referred in some of the references of available papers [2]. This makes zirconolite potentially ideal for sequestering the radioactive elements present in spent nuclear fuel over the millennia required for them to decay into less harmful substances.

Cerium is often used as a substitute for plutonium in studies of nuclear waste ceramics. Cerium and plutonium have very close ionic radii (Ce^{4+} = 97 pm and Pu^{4+} = 96 pm) when coordinated by eight other atoms [8], as in the Ca site in zirconolite [1]. However, cerium is far safer to work with than plutonium.

Lumpkin [1] compared several mineral phases for waste immobilisation. The advantages of zirconolite over others include its high aqueous durability and chemical flexibility, though it is less tolerant to radiation dose than some other phases. The relative aqueous stability of several phases from pH 2–12 is as follows: zirconolite > pyrochlore > brannerite >> perovskite [1].

Brannerite is known to dissolve quickly in sulphuric and hydrochloric acids under oxidising conditions [9,10], while betafite (pyrochlore) will dissolve at a lower rate under similar conditions [11]. By comparing the leaching of zirconolite with the leaching of brannerite and betafite under these conditions, the stability of zirconolite as a host for actinides can be evaluated and demonstrated.

2. Materials and Methods

2.1. Sample Preparation

Synthetic zirconolite samples were prepared using two different methods. The zirconolite target composition was $Ca_{0.75}Ce_{0.25}ZrTi_2O_7$, with Ce as a substitute for Pu. Assuming that the feed mixtures are homogeneous, the composition of the feed mixtures for both methods should be CaO 11.5 wt. %, Ce_2O_3 11.2 wt. %, ZrO_2 33.7 wt. %, and TiO_2 43.6 wt. %. The oxidation state of Ti was expected to be mixed 4/3+ to maintain charge balance. The preparation methods are outlined below.

   i.   Alkoxide route

Required quantities of zirconium n-propoxide and titanium isopropoxide were hydrolysed with a solution containing the necessary amounts of calcium and cerium nitrate. The slurry was then stir-dried in a stainless steel beaker on a hot plate. Once dried the product was calcined at 750 °C in air for 8 h.

   ii.   Oxide route

ZrO_2 and TiO_2 as approximately 1 μm particle size powders, CeO_2 as a 5 μm particle size powder and calcium nitrate were combined to form a slurry. This was stir dried and calcined as for the alkoxide route.

The powders produced by both routes were then planetary milled as a slurry for 20 min with propan-2-ol as a carrier fluid, dried and sieved. The powders were then blended with 2.2 wt% Ti metal in a Turbula mixer and packed into stainless steel hot isostatic pressing (HIP) cans 3.5 cm diameter by 5 cm high. The Ti metal acted as an in-can reducing agent to convert Ce^{4+} to Ce^{3+} and Ti^{4+} to Ti^{3+} to ensure correct charge balance in the zirconolite. The HIP cans were then sealed and evacuated, and then hot isostatically pressed at 1320 °C and 100 MPa for 2 h.

2.2. Sample Characterisation

Mineralogical analysis by X-ray diffraction (XRD) was performed with a GBC Enhanced Multi-material Analyser (EMMA) (GBC Scientific Equipment, Braeside, Victoria, Australia) at Murdoch

University. Samples were placed directly onto X-ray absorbing silicon discs within circular metal sample holders. Samples were introduced under a drop of ethanol and the ethanol was allowed to evaporate prior to the analysis.

The X-ray tube was operated at a voltage of 35.0 kV and current of 28.0 mA. Diffraction patterns were collected over a range of $20° ≤ 2\theta ≤ 70°$ using a 1° diverging slit, a 0.2° receiving slit and a 1° scattering slit. A step size of 0.02° was used, with a speed of 1°/min (1.2 s per step) with five passes. Cu Kα X-rays were used. A Kα_2 strip was performed on the diffraction patterns, with a Kα_2/Kα_1 ratio of 0.51. Initial scans showed no peaks of interest below 20°.

Scanning electron microscopy (SEM) observations were performed with a JEOL JCM-6000 bench top SEM with an energy dispersive X-ray spectroscopy (EDX) analyser (JEOL Ltd., Tokyo, Japan). An accelerating voltage of 15 kV was used to produce the SEM images of the samples. Both secondary electron (SE) and backscattered electron (BSE) modes were utilised. Particles were mounted on carbon discs. The cross-sections of the particles were prepared by embedding in epoxy resin and subsequent polishing with silicon carbide. A 15 kV accelerating voltage was used for the semi-quantitative EDX analyses, the highest possible with the instrument used in this study. All EDX analyses were run for 60 s. All images associated with EDX analyses were taken in BSE. For line-scan analyses, the counting time was set to 15 s per step. X-ray elemental maps were produced with a resolution of 384 × 512 pixels and a counting time of 10 × 0.2 ms per pixel. The standard colour scheme for the element maps adhered to throughout this report is red for calcium, green for zirconium and blue for titanium. Cerium was not included on the element maps due to the overlap of the Ce Lα peak at 4.83 keV with the Ti Kβ peak at 4.93 keV.

All aqueous samples were analysed for calcium, titanium, zirconium and cerium with a Thermo-Fisher iCAP-Q ICP-MS instrument (Thermo-Fisher Scientific, Bremen, Germany) at Murdoch University. The purity of zirconolite samples was verified by digestions and ICP-MS analysis performed at a commercial minerals laboratory. The coarse zirconolite was assayed twice.

2.3. Leaching Study

Similar conditions for the leaching study were used to those previously reported for brannerite leaching [9,10,12]. Acid (HCl, H$_2$SO$_4$) leaching experiments were run for five hours and alkaline leaching tests were run for 24 h to enable comparison with brannerite leached under the same conditions. Coarse zirconolite was used in the majority of the experiments. The highest temperature experiment for each lixiviant was repeated with fine zirconolite. The conditions used in the leaching experiments are listed in Table 1.

Table 1. Leaching conditions used in this study.

Lixiviant	Temperature (°C)	Lixiviant Concentration (mol/L)	Size Range (μm)	Duration (h)
HCl	50	0.25	125–250	5
HCl	85	0.25	125–250	5
HCl	50	1.00	125–250	5
HCl	85	0.25	63–125	5
H$_2$SO$_4$	30	0.25	125–250	5
H$_2$SO$_4$	50	0.25	125–250	5
H$_2$SO$_4$	70	0.25	125–250	5
H$_2$SO$_4$	85	0.25	125–250	5
H$_2$SO$_4$	50	1.00	125–250	5
H$_2$SO$_4$	85	0.25	63–125	5
NaHCO$_3$, Na$_2$CO$_3$	70	0.67, 0.33	125–250	24
NaHCO$_3$, Na$_2$CO$_3$	70	0.67, 0.33	63–125	24

As with the brannerite leaching experiments, Fe^{3+} was added as an oxidant. Iron was added as 0.05 mol/L $FeCl_3$ in the chloride leaching experiments, 0.05 mol/L $Fe(SO_4)_{1.5}$ in the sulphate leaching experiments and 0.025 mol/L $K_3Fe(CN)_6$ in the carbonate leaching experiments.

3. Results and Discussion

3.1. Feed Characterisation

The two feed samples produced using the different methods had different size distributions—63–125 μm for the alkoxide route sample and 125–250 μm for the oxide route sample. Wet screening was used to narrow down the size range of each sample. These are labelled 'fine' sample and 'coarse' sample, respectively.

3.1.1. Feed Assays

Chemical analyses of the synthetic zirconolite by ICP-MS presented in Table 2; Table 3 show that the synthetic zirconolite from both methods was of high purity. Hafnium was the main non-formula element identified. Hafnium is often found with zirconium, and separating the two presents a significant technical challenge.

Table 2. Major elements (>0.1 wt%) in the zirconolite feed samples.

Element	Coarse Zirconolite	Fine Zirconolite
Zr	25.88%	25.54%
Ti	25.75%	25.68%
Ce	8.20%	8.12%
Ca	7.83%	7.88%
Hf	0.63%	0.63%
Si	0.19%	0.25%

Table 3. Minor elements (>100 ppm) in the zirconolite feed samples in ppm.

Element	Coarse Zirconolite	Fine Zirconolite
Na	800	900
Ag	707	849
Nb	650	620
Fe	475	645
Mg	355	420
S	350	400
Al	280	430
P	245	240
Ga	240	275
K	200	300

These zirconolite specimens had average formulas of $Ca^{2+}_{0.71}Ce^{3+}_{0.21}(Zr_{1.03}Hf_{0.01})Ti_{1.95}O_7$ for the coarse zirconolite and $Ca^{2+}_{0.72}Ce^{3+}_{0.21}(Zr_{1.02}Hf_{0.01})Ti_{1.95}O_7$ for the fine zirconolite. Si has been excluded based on EDX results, showing that it was present in a separate minor SiO_2 phase. Both were slightly Ti deficient compared to the ideal zirconolite composition, but had a higher amount of Ti than typical natural samples. Titanium is commonly replaced by Fe^{3+}/Nb^{5+} in natural zirconolite. Tantalum may also be present in this site in small amounts [13] Cerium, REEs and actinides replace calcium in the zirconolite crystal structure [2,4,14–16].

3.1.2. XRD

XRD also showed feed samples produced by both methods to be effectively pure zirconolite, a solid solution $(Ca_{0.75}Ce_{0.25})ZrTi_2O_7$. The XRD data showed the presence of zirconolite and perovskite

as major phases. Zirconolite exists in three polytypes [17]; and reference diffraction patterns for them have been superimposed on the measured diffraction pattern (Figure 1). Titanium dioxide (rutile) was detected in small amounts. The other polymorphs of titanium dioxide, anatase and brookite, were not detected. Perovskite was detected as a minor phase.
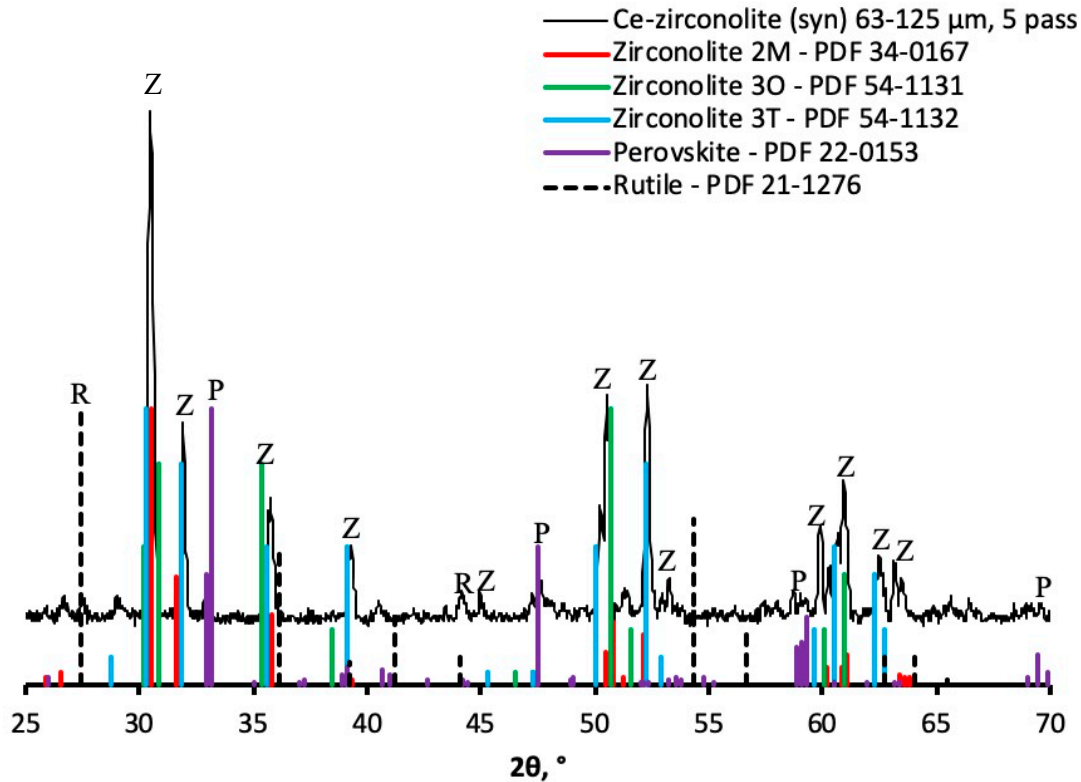

Figure 1. X-ray diffraction (XRD) pattern of the zirconolite material with relevant PDF references.

3.1.3. SEM, EDX

The examination by SEM showed the feed samples contained very small inclusions of a second phase, and possibly some unreacted ZrO_2. Backscattered electron images (Figure 2) showed that the inclusions have a lower average atomic mass. EDX analyses (Figures 3 and 4) indicated that this material was titanium dioxide, though it is not possible to tell from the EDX analyses which polymorph of titanium dioxide was present. The XRD results indicate that it was most likely rutile, possibly a relic of the Ti metal added for redox control during the HIP process. Neither silicon nor hafnium were detected in EDX analyses of zirconolite. When silicon was detected, it occurred as a separate phase (SiO_2), while hafnium at 0.6% of the mass was below the detection limit for EDX analyses.
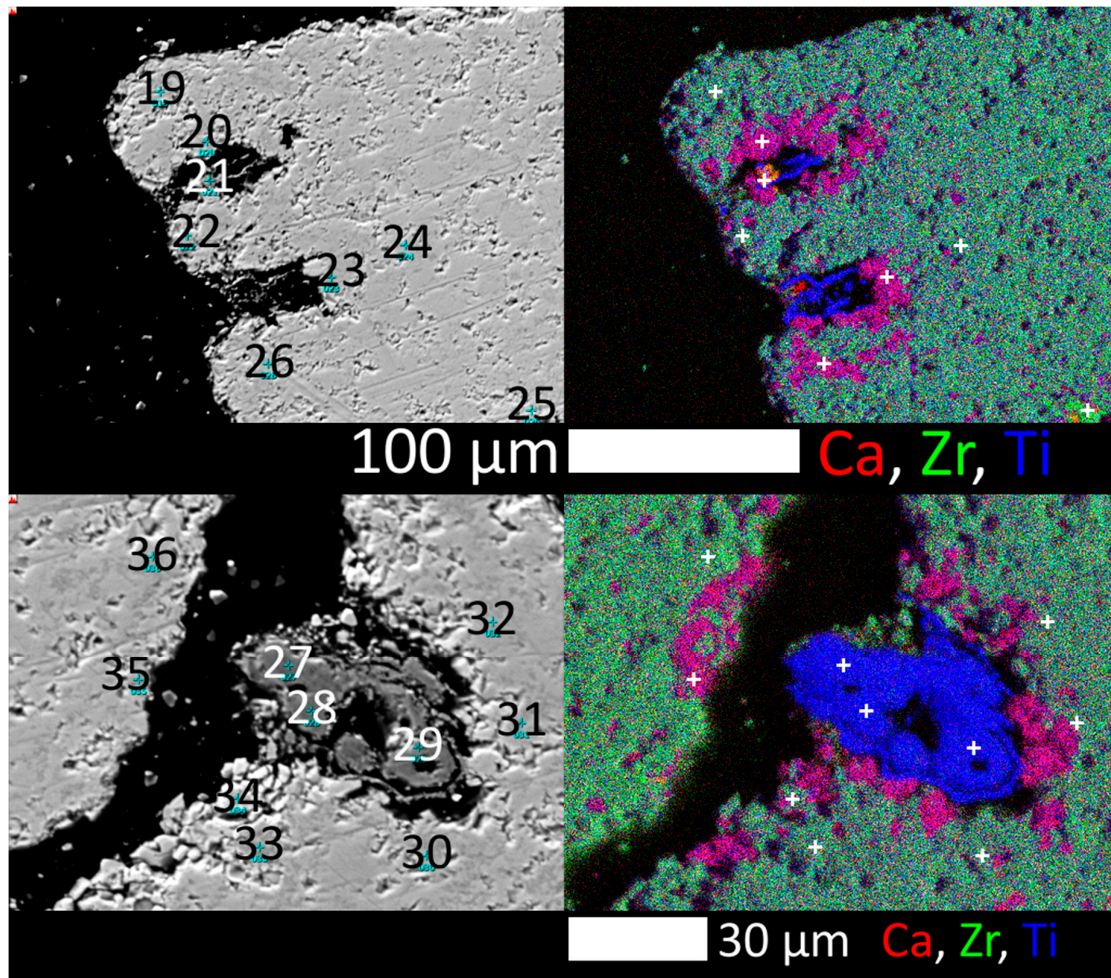
Figure 2. Rutile inclusions within zirconolite grains surrounded by perovskite. **Left**: backscattered electron (BSE) images, **right**: element map.
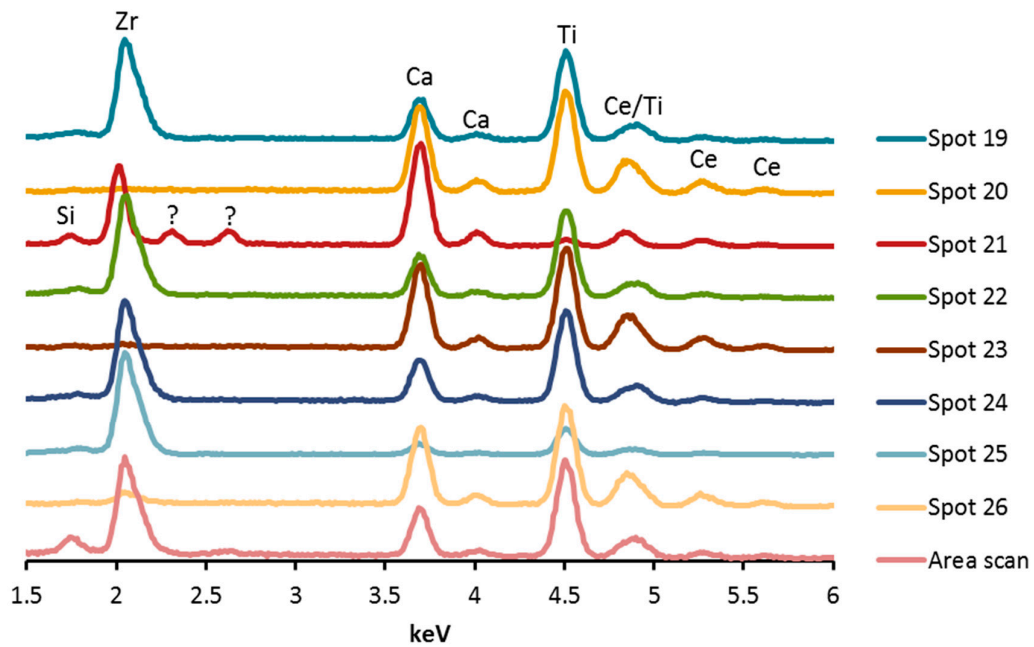
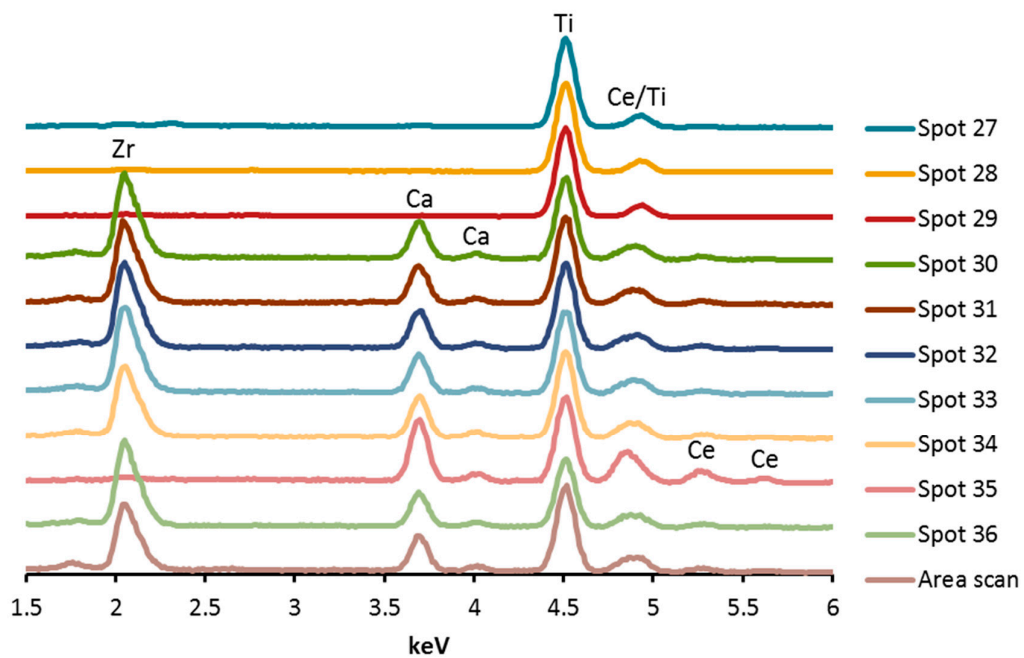**Figure 3.** Spectra of spots analysed in the top half of Figure 2.

Figure 4. Energy dispersive X-ray spectroscopy (EDX) spectra of spots analysed in the bottom half of Figure 2.

EDX analyses of the zirconium-free regions showed that they contained cerium along with calcium and titanium (Figures 3 and 4). This material was probably the same perovskite phase identified by XRD. The brightness of this phase in the BSE images suggests that was not pure Ca perovskite however. Pure Ca perovskite has a low average atomic number (Z_{avg}) (16.5) close to that of rutile (16.4) [18] while the calculated Z_{avg} of zirconolite exceeds 22. While there were some subtle variations in the BSE brightness of the zirconolite/perovskite regions, these variations did not clearly correlate with variations in composition as determined by EDX spectra or elemental maps.

It is difficult to resolve the cerium Lα peak from the titanium Kβ peak. For this reason, cerium was not included on any of the element maps. Closer examination shows the Ce Lβ peaks in some spectra allowing the presence of cerium to be confirmed. Of all the spots analysed on the feed sample, cerium was most prominent in the spectrum of spot 35 in Figure 4.

Eight oxygen atoms coordinate the calcium site in zirconolite, but the calcium site in perovskite is larger and coordinated by 12 oxygen atoms [19]. Hence, calcium within perovskite undergoes extensive isomorphous substitution with uranium, thorium and REEs [20]. Perovskite is commonly formed as a side-product in the synthesis of zirconolite and other titanate ceramics [14,21] and is an intentional phase in Synroc C, to host Sr-90. Studies on polyphase heterogeneous actinide titanate ceramics show that large lanthanide ions like Ce^{3+}/Nd^{3+} and trivalent actinides (Pu^{3+}, Am^{3+}, Cm^{3+}) favour the Ca site of perovskite over zirconolite. This explains the presence of cerium in the perovskite phase in this sample. The partition coefficient between zirconolite and perovskite was lower for larger cations [21].

Zirconolite is significantly more stable than perovskite [1,8]; thus, the formation of perovskite in synthetic samples intended for uranium sequestration should be minimised as much as possible. Pöml et al. [14] succeeded in synthesising a cerium doped zirconolite without detectable levels of perovskite by adding a stoichiometric excess of ZrO_2 during synthesis.

Along with the three major separate phases, rutile, Ce-perovskite and Ce-zirconolite, one of the spectra indicates the presence of a fourth minor Zr oxide phase (spot 25 in Figure 3). The boundaries between phases in the coarse zirconolite sample are clear and distinct unlike those observed in brannerite [22]. The boundaries between phases in this sample are clear and distinct unlike those observed in natural brannerite [22], as is apparent from EDX line analyses across a rutile inclusion. Rutile inclusions were typically surrounded by smaller perovskite inclusions though not all perovskite inclusions were associated with rutile.

3.2. Leaching Kinetics

Under similar leaching conditions, the synthetic zirconolite dissolved much more slowly than natural brannerite [9,12,23] and betafite [11,24,25]. Cerium extraction from zirconolite followed linear kinetics in sulphuric acid (Figure 5). After five hours of leaching, cerium extraction had yet to plateau. Titanium dissolved at a slower rate than cerium but faster than zirconium. This suggests that zirconolite is not dissolving in significant amounts. Based on the observed leaching kinetics, perovskite is more susceptible to leaching than zirconolite. Calcium extraction kinetics were not included due to the significant levels of analytical error in measuring the calcium concentrations in solution. Apart from Ca, these results are consistent with earlier work that showed the typical order of elemental dissolution rates from zirconolite in acidic solutions is Ca > Ce > Ti > Zr [14].
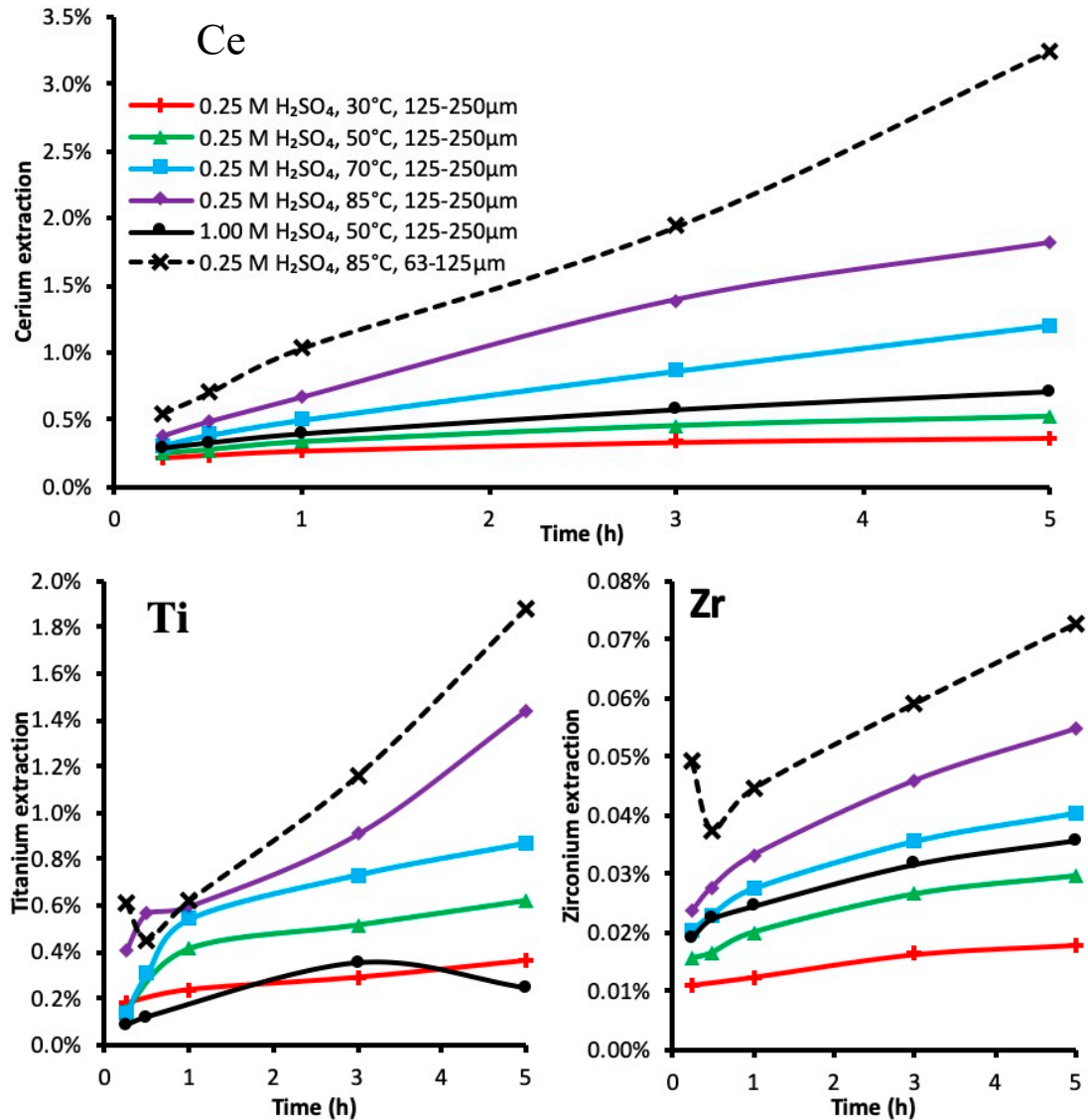
Figure 5. Leaching kinetics under various conditions in sulphuric acid media.

Similar trends were apparent during leaching in chloride media (Figure 6) to those observed for sulphate media. Cerium dissolved faster than titanium, which in turn dissolved faster than zirconium. While extraction rates were lower in chloride media compared to sulphate media at the same temperature and acid concentration, variations in acid concentration had a larger effect on the rate of dissolution in chloride media. Both of these behaviours have been observed when leaching brannerite in chloride and sulphate media over a wide range of temperatures and acid concentrations [10]. The order of uranium and titanium extraction from brannerite was approximately 0.5 with respect to H_2SO_4 while the order was approximately 1 with respect to HCl [9,10].
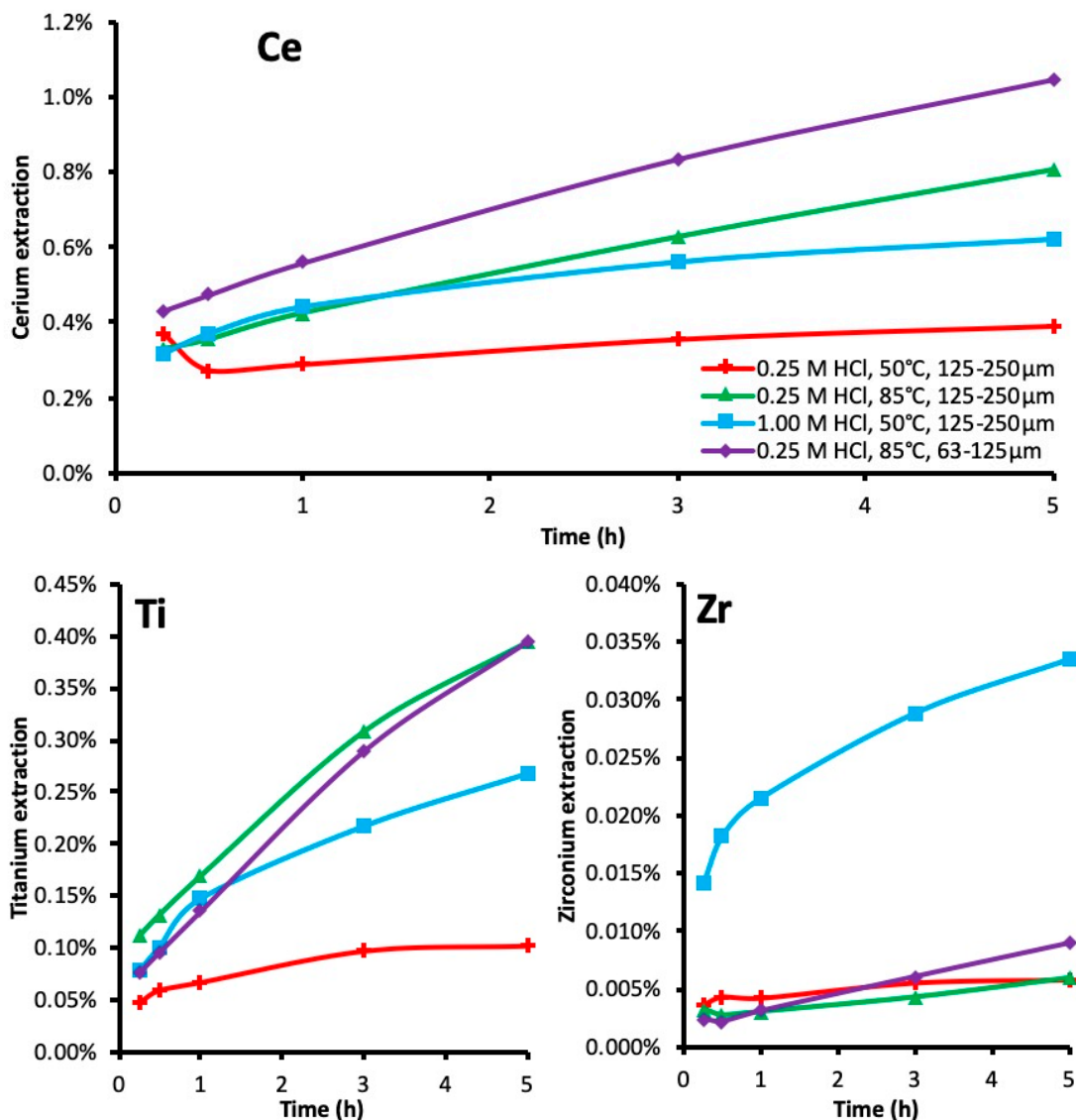
Figure 6. Leaching kinetics under various conditions in hydrochloric acid media.

After five hours of leaching, the extent of cerium dissolution was 3–6 times higher than that of titanium in hydrochloric acid and around 100 times higher than that of zirconium in 0.25 M HCl. In 1.00 M HCl, the Ce/Zr ratio decreased to approximately 20, with acid concentration having a significant effect on the dissolution rate of zirconium in chloride media. These trends match those observed in long term leaching studies on synthetic actinide waste forms such as zirconolite and pyrochlore at pH 2 in 0.01 M HNO_3 solution [26], and are in agreement with the relative solubility of the simple oxides of these elements (Figure 7; Reactions 1–5).
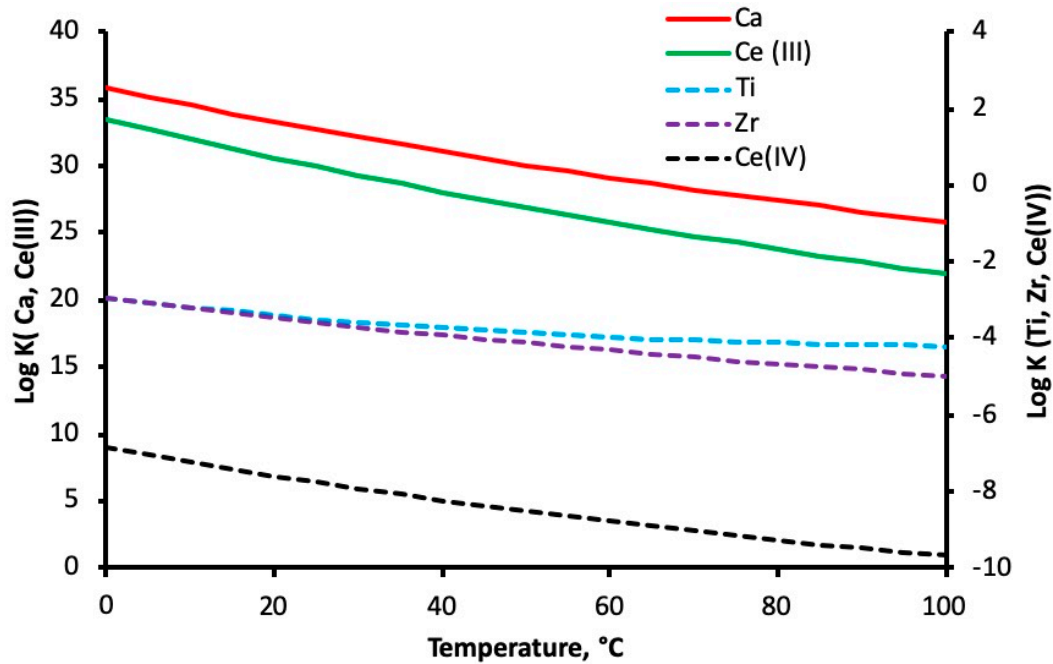
Figure 7. Solubilities of simple oxides of Ca, Ce, Ti and Zr from 0–100 °C as calculated using software [27]. Log K values for Reactions 1–5 were used.

Ca	$CaO + 2\,H^+ \rightarrow Ca^{2+} + H_2O$	Reaction 1
Ce(III)	$0.5\,Ce_2O_3 + 3\,H^+ \rightarrow Ce^{3+} + 1.5\,H_2O$	Reaction 2
Ce(IV)	$CeO_2 + 4\,H^+ \rightarrow Ce^{4+} + 2\,H_2O$	Reaction 3
Ti	$TiO_{2(rutile)} + 2\,H^+ \rightarrow TiO^{2+} + H_2O$	Reaction 4
Zr	$ZrO_2 + 2\,H^+ \rightarrow ZrO^{2+} + H_2O$	Reaction 5

The relative rates of leaching were different in an alkaline environment (Figure 8). As with the acid leaching experiments, rates of dissolution in alkaline media were significantly slower than those observed for brannerite. Titanium dissolved faster than cerium, which dissolved much faster than zirconium. If the zirconolite was allowed to react for longer, it is expected that titanium would re-precipitate as titanium dioxide as observed with brannerite and Ti rich uranium ore [12,28]. Titanium is somewhat amphoteric and may dissolve as Ti(OH)$_5^-$ at high pH [29,30].
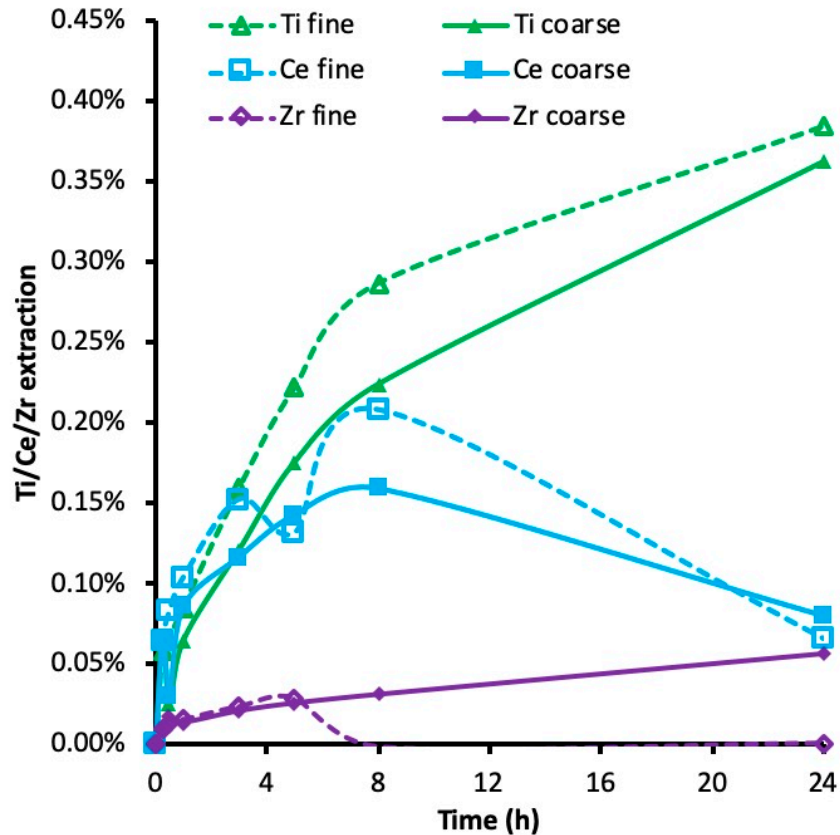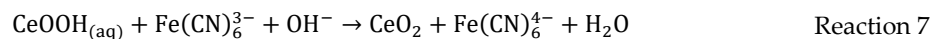
Figure 8. Extraction of titanium, zirconium and cerium from zirconolite in alkaline media at 70 °C.

While Ce_2O_3 will readily dissolve in acidic or neutral conditions, CeO_2 is far less soluble (Figure 7). Oxidising conditions may have caused cerium as Ce^{3+} or $CeOOH$ to be oxidised to insoluble CeO_2. Calculations [26] have indicated that this process is favourable (see Reactions 6 and 7). Increasing the pH will make Reaction 7 even more favourable.
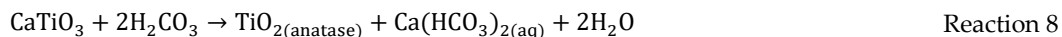
$$0.5\ Ce_2O_3 + 0.5\ H_2O \rightarrow CeOOH_{(aq)}$$ Reaction 6

$$\Delta_{rxn}G^{70°C} = -25.0\ kJ/mol$$

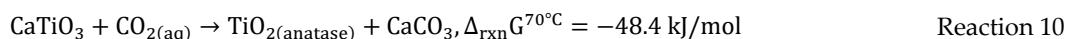$$CeOOH_{(aq)} + Fe(CN)_6^{3-} + OH^- \rightarrow CeO_2 + Fe(CN)_6^{4-} + H_2O$$ Reaction 7

$$\Delta_{rxn}G^{70°C} = -129.4\ kJ/mol$$

While the unreliability of the calcium assay data makes it impossible to determine its behaviour in solution, secondary calcite phases have been observed when leaching brannerite (~2% Ca) under similar conditions [12]. The leaching of calcium from perovskite in carbonate solutions forming anatase and calcite has been observed in natural titanium deposits [31]. The process may take place according to the following reactions:

$$CaTiO_3 + 2H_2CO_3 \rightarrow TiO_{2(anatase)} + Ca(HCO_3)_{2(aq)} + 2H_2O$$ Reaction 8

$$Ca(HCO_3)_{2(aq)} \rightarrow CaCO_3 + CO_2 + H_2O$$ Reaction 9

The overall process is described in Reaction 10:

$$CaTiO_3 + CO_{2(aq)} \rightarrow TiO_{2(anatase)} + CaCO_3, \Delta_{rxn}G^{70°C} = -48.4\ kJ/mol$$ Reaction 10

Clearly, this process is favourable under these conditions.

3.3. Activation Energy

The rate of cerium dissolution showed a strong dependence on temperature. The average rate of dissolution between 1 and 5 h residence time was used to calculate the activation energy in the temperature range 30 to 85 °C, shown in Table 4. This can be considered to be the initial rate of

extraction given the long periods over which zirconolite is known to dissolve [14,26]. Arrhenius plots for the sulphate leaching experiments showing data from tests conducted at 30, 50, 70 and 85 °C are shown in (Figure 9).
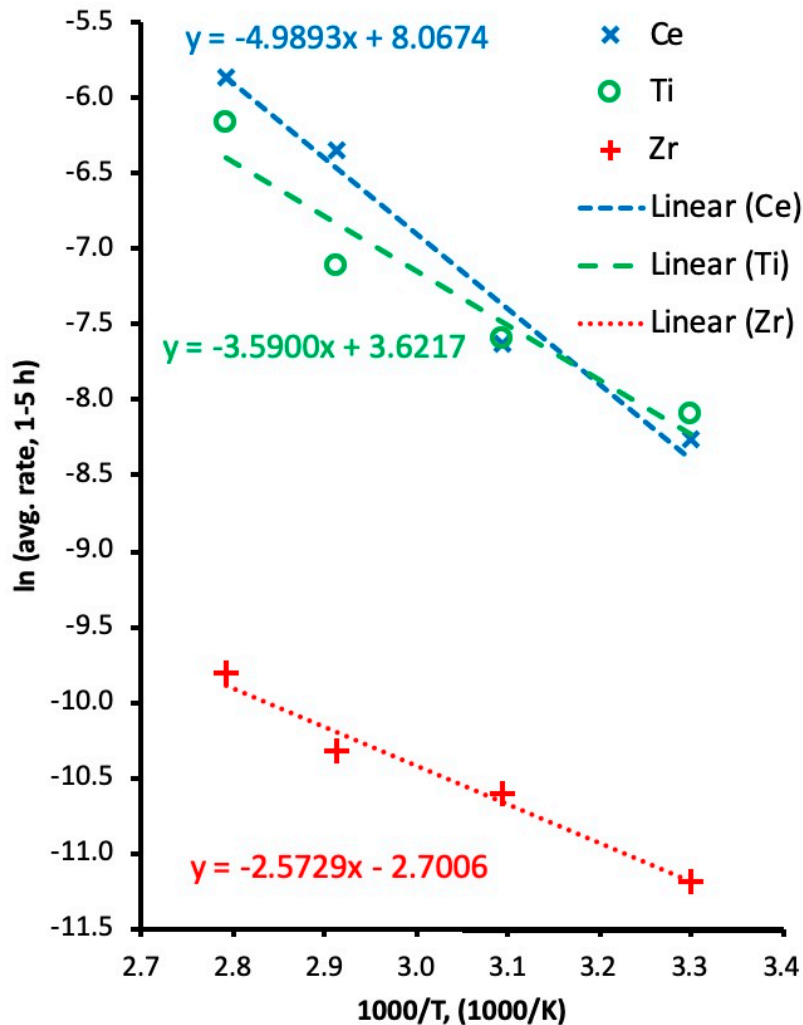

Figure 9. Arrhenius plot for Ce, Ti and Zr leaching in 0.25M H_2SO_4, based on the average rate of leaching from 1–5 h.

Activation energies (Table 4) were also calculated for the hydrochloric acid leaching tests, though the results are less certain as chloride leaching was only done at two temperatures, 50 and 85 °C. Arrhenius plots may have multiple regions corresponding to different rate determining steps [32], thus, such plots derived from only two temperature points may be unreliable.

Table 4. Activation energy (kJ/mol) for the dissolution of Ce, Ti and Zr based on extraction rates from 1–5 h.

Element	H_2SO_4	HCl
Ce	41.5	35.5
Ti	29.8	50.2
Zr	21.4	15.4

Omitting the outlying 85 °C point from the titanium calculation gives an activation energy of 21.4 kJ/mol in sulphate media, very close to the calculated activation energy for zirconium dissolution in the same media, possibly indicative of a similar dissolution mechanism.

Longer term leaching experiments over 14 days in 1 M HCl at 100–200 °C gave an activation energy of approximately 20 kJ/mol for the dissolution of cerium and titanium from synthetic zirconolite [14]. Leaching experiments with similar synthetic samples by Zhang et al. [33] between 25 and 75 °C and over a pH range of 2–12, showed that the activation energy for uranium release from zirconolite varied with pH when these calculations were repeated with data presented by Zhang et al. [33]. The activation energy for uranium release was typically 15–20 kJ/mol with the one outlier being the pH 4.1 tests which gave a calculated activation energy value of 37 kJ/mol.

Comparisons with other studies [9,10] showed that zirconolite underwent slower dissolution than brannerite or even betafite when leached under similar conditions (Figure 10).
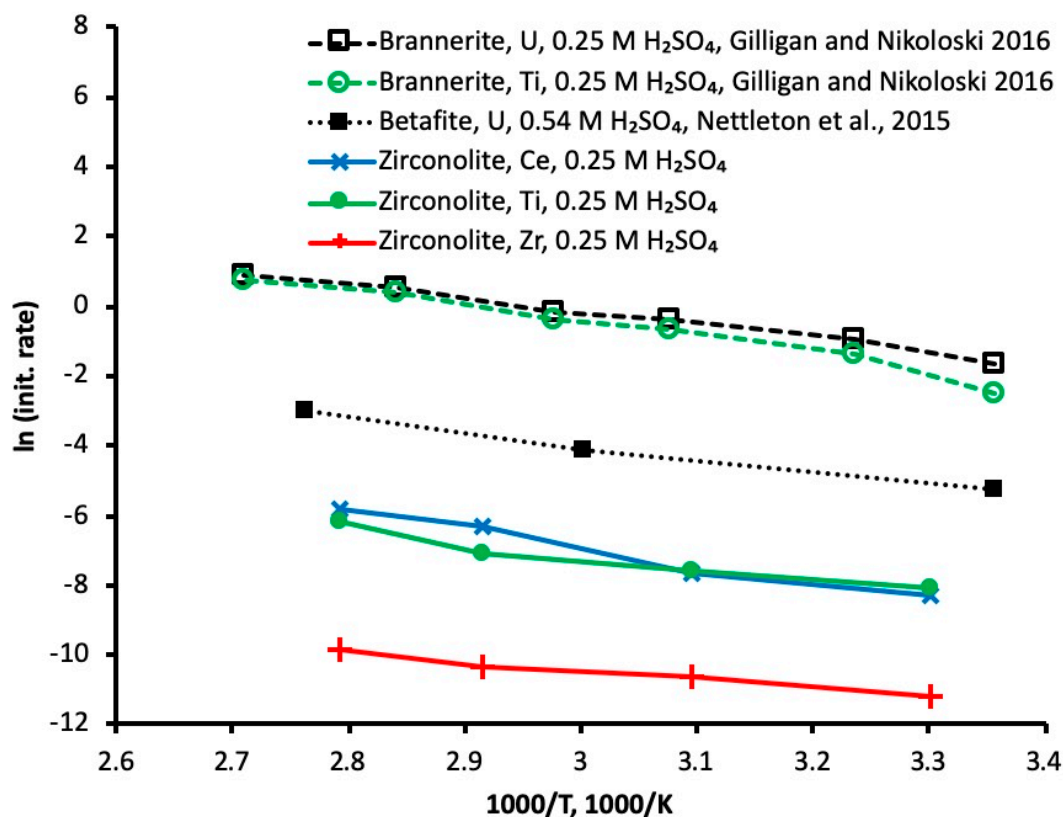

Figure 10. Arrhenius plots for the extraction of various elements from brannerite, betafite and zirconolite in sulphuric acid.

3.4. Leached Residue Characterisation

Unlike the brannerite studied previously, there were few apparent signs of corrosion after the leaching of zirconolite. Images, element maps and spectra were taken of zirconolite particles leached at the highest temperature in each lixiviant.

Figure 11 shows a rutile inclusion surrounded by perovskite following chloride leaching. It is possible that the perovskite regions may have undergone some corrosion. There was no sign of pitting on the zirconolite (light green in all element maps) visible at the resolution of these images, though line analyses indicated that the outermost 2–5 μm were enriched in titanium and zirconium and depleted of calcium and cerium relative to the core of the particles.

These apparent changes in the distribution of elements in the solid phase are corroborated by the leaching kinetics data, which showed that the extraction of cerium was consistently higher than that of titanium and significantly higher than that of zirconium (Figures 5 and 6).
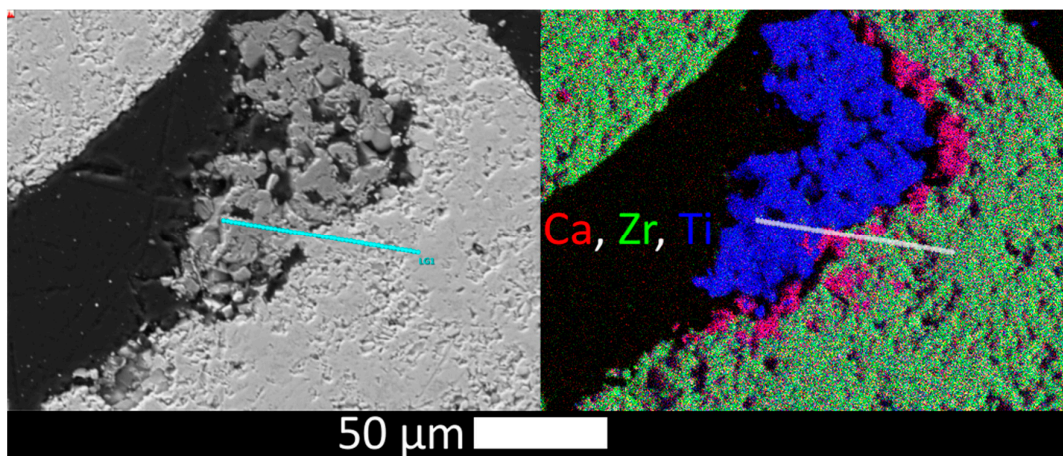

Figure 11. Grain boundary in zirconolite after leaching in 0.25 M HCl at 85 °C. **Left**: BSE image, **right**: element map.

There were less visible signs of corrosion in the sulphate leaching system (Figure 12), although line EDX analyses indicate some selective leaching of calcium and cerium in the outermost 2–5 μm layer of zirconolite. Line A intersects a rutile inclusion and a perovskite grain, while line B runs across a protrusion of zirconolite corroded on both sides, both ends showing decreased Ca/Ce relative to Ti/Zr. There were no visible signs of corrosion on the rutile inclusions. Past experience with ilmenite [34] suggests minimal corrosion occurs in 0.25–1.00 M H_2SO_4 at 95 °C during 5 h of contact.
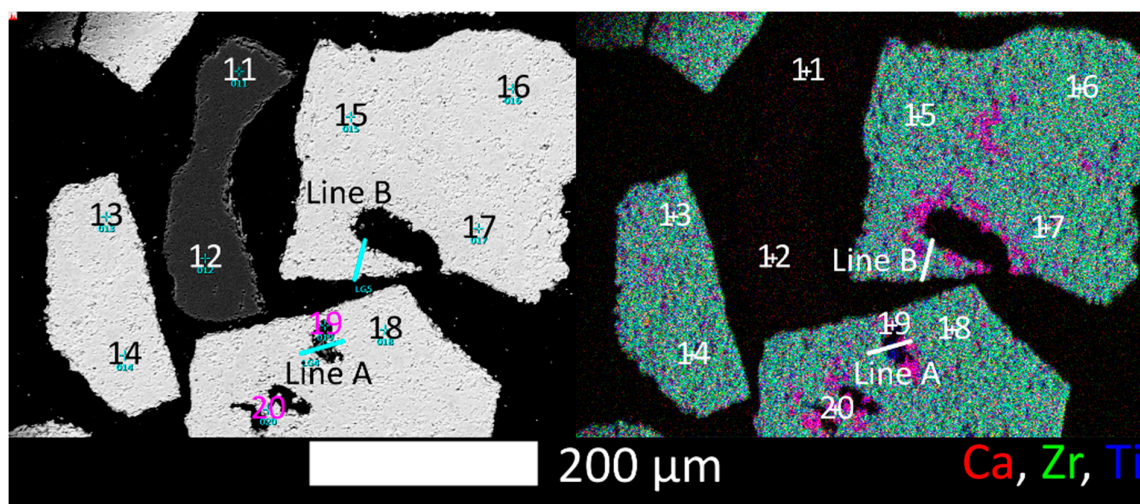

Figure 12. A large zirconolite particle with rutile inclusions after leaching in 0.25 M H_2SO_4 at 85 °C for 5 h Left: BSE image, right: element map.

There were minimal signs of corrosion in carbonate leaching media (Figures 13 and 14). Once again, this is consistent with the leaching kinetics (Figure 8) and past experience with brannerite [12,28].
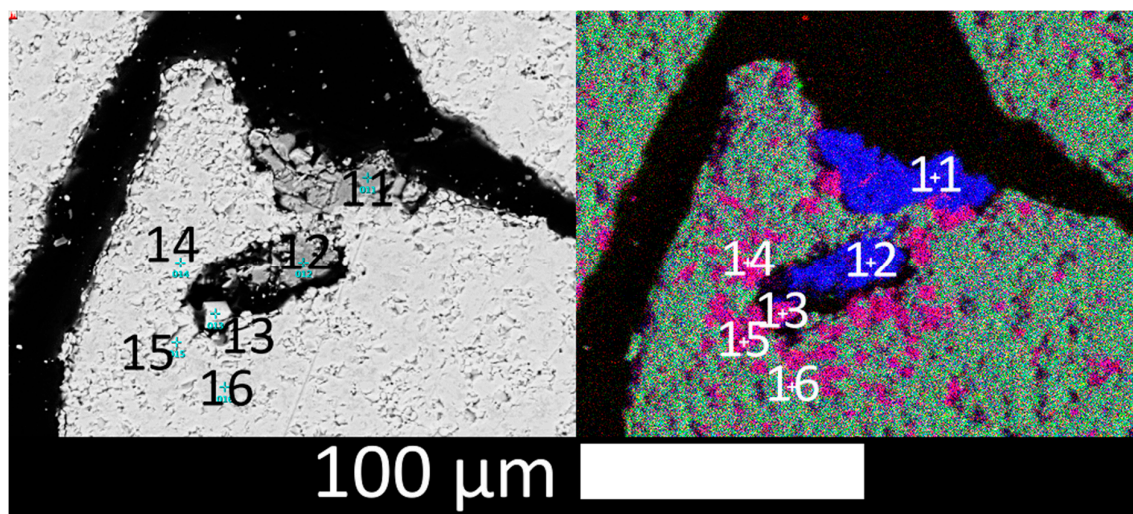
Figure 13. Backscattered electron SEM image (left) and Ca–Zr-Ti map (right) of zirconolite after 24 h of leaching in sodium carbonate at 70 °C with the locations of EDX analyses. Spectra are shown in Figure 14.
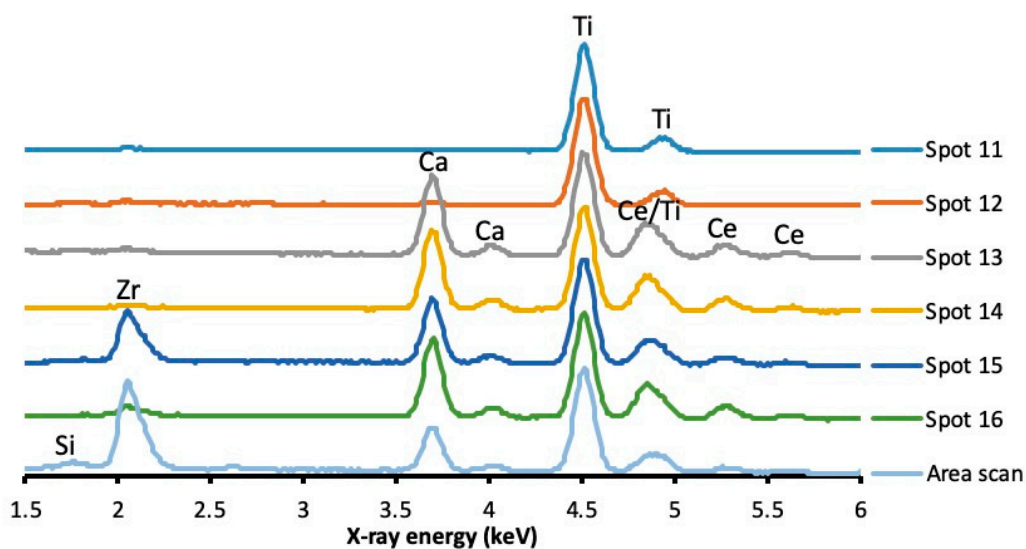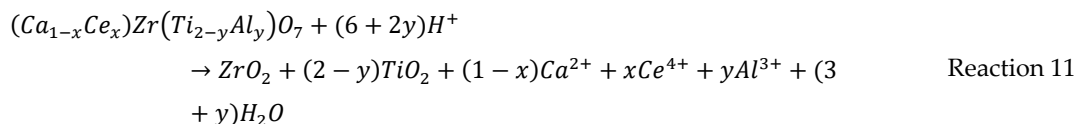

Figure 14. EDX spectra of rutile and perovskite inclusions in a zirconolite particle after leaching in sodium carbonate.

The alteration of zirconolite to secondary phases such as anatase and baddeleyite has been observed in earlier work [14,33]; however, these leaching tests typically ran over longer time periods of at least two weeks.

3.5. Reaction Mechanisms

Particle size had a clear effect on the rate of cerium dissolution in sulphate and chloride media. The rate at which various elements dissolve from zirconolite has been observed to be proportional to the surface area in contact with the lixiviant until saturation is reached and secondary phases begin to form [14]. The extraction rates of titanium and zirconium were less affected by particle size (Figure 5; Figure 6), as might be expected if they were forming secondary phases.

Calcium, aluminium and cerium dissolution were proportional to surface area, while zirconium and titanium were observed to plateau due to the formation of secondary solid phases on reaching saturation [14]. The reaction for zirconolite dissolution given by Pöml et al. [14] is:

$$(Ca_{1-x}Ce_x)Zr(Ti_{2-y}Al_y)O_7 + (6+2y)H^+$$
$$\rightarrow ZrO_2 + (2-y)TiO_2 + (1-x)Ca^{2+} + xCe^{4+} + yAl^{3+} + (3 \qquad \text{Reaction 11}$$
$$+ y)H_2O$$

Titanium and zirconium precipitation does not occur until ZrO_2 and TiO_2 exceed saturation at the zirconolite-solution interface [14]. These experiments were not run for long enough for the zirconium and titanium concentrations in the bulk solution to plateau, though the outer 5 μm of zirconolite leached in sulphate media at 85 °C was enriched in titanium and zirconium indicating that saturation may have been reached at the solid-aqueous interface. The relative rates of extraction observed in this study matched those identified in longer term leaching studies [14,26].

It is under oxidising conditions that the similarities between cerium and plutonium break down. Cerium is oxidised to insoluble CeO_2 (Reaction 7), while insoluble PuO_2 can be oxidised further and remobilised as PuO_2^+ and PuO_2^{2+} complexes [35], similar to what is typically seen with uranium.

3.6. Crystallinity and Leachability

There are two reasons for the much lower extent of dissolution observed in the zirconolite leaching compared with earlier work with brannerite. Zirconolite is known to be highly chemically stable. This sample is also highly crystalline as is apparent from the XRD results (Figure 1). Crystalline phases are more refractory than metamict materials [2,23]. Even within the same mineral sample, heavily altered metamict zones are more susceptible to corrosion than less altered zones [22].

The process of metamictisation, by which a radioactive crystalline material gradually becomes amorphous from internal irradiation [36] decreases its chemical and physical stability [14]. However, if a metamict material is recrystallised by heating, the material becomes less soluble. This has been documented for brannerite [23], betafite [11] and synthetic zirconolite [26].

Synthetic titanates have been synthesised with plutonium-238 (half-life = 87.7 years) to study the rate and effects of radiation damage over the course of five years. Strachan et al. [26] showed that the degree of radiation damage has little to no effect on the chemical stability of zirconolite and pyrochlore. Similarly, studies of natural zirconolites have shown them to be highly chemically durable having survived 600 Ma or more in nature [2]. This means that measurements of the chemical stability of zirconolite based on recently prepared non-metamict samples are likely to be applicable to aged and metamict samples as well. Furthermore, this indicates that zirconolite is a good material to use for the long-term sequestration of radioisotopes.

The minor perovskite phase seemed to have undergone more corrosion than the surrounding zirconolite phase. This could be related to the formation of Ce^{3+}, which is easy to form, as observed in the fabrication, and is what stabilises perovskite. Perovskite should be avoided when synthesising zirconolite, as this may increase the proportion of soluble and mobile plutonium. Pöml et al. [14] achieved this by adding a stoichiometric excess of ZrO_2. However, this is likely to be less of a concern for the immobilisation of tetravalent actinide ions.

In addition to long term durability in the disposal environment, a wasteform for fissile material immobilisation must demonstrate proliferation resistance such that the fissile material cannot be retrieved by dissolution of the wasteform. When the United States Department of Energy was developing wasteform options for the disposition of surplus weapons grade plutonium, zirconolite, the initial choice of wasteform, was replaced by betafite (therein referred to as pyrochlore) on the grounds that the U–238 in the wasteform would guard against certain long term criticality events in the disposal environment [37]. This study, in conjunction with our previous work on betafite leaching, strongly indicates that the addition of depleted uranium to the wasteform is detrimental to proliferation resistance. Given the demonstrated durability of zirconolite, from both natural and synthetic samples, long term criticality risks in the disposal environment seem a remote possibility,

and this supports the selection of zirconolite, above betafite, as the wasteform for disposition of surplus plutonium.

4. Conclusions

Synthetic zirconolite is significantly more stable than natural brannerite or betafite. The most intense conditions used in this study did not cause synthetic zirconolite to undergo significant leaching or visible corrosion despite the same conditions being sufficient for near complete dissolution of natural brannerite in under five hours [9,12,22].

There was some evidence for incongruent dissolution, as the outer 5 μm of some leached zirconolite particles were enriched in titanium and zirconium, indicating that these elements had exceeded saturation at the aqueous-solid interface.

Fine zirconolite dissolved faster than the coarse material, indicating that the rate of dissolution is related to surface area. In practice, the rate of dissolution could therefore be further minimised by forming the zirconolite waste ceramics into larger solid masses.

References

1.　Lumpkin, G.R. Ceramic waste forms for actinides. *Elements* **2006**, *2*, 365–372.
2.　Lumpkin, G.R. Alpha-decay damage and aqueous durability of actinide host phases in natural systems. *J. Nucl. Mater.* **2001**, *289*, 136–166.
3.　Gieré, R; Williams, C.T. REE-bearing minerals in a Ti-rich vein from the Adamello contact aureole (Italy). Contrib. *Min. Pet.* **1992**, *112*, 83–100.
4.　de Hoog, J.C.M.; van Bergen, M.J. Notes on the chemical composition of zirconolite with thorutite inclusions from Walaweduwa, Sri Lanka. *Mineral. Mag.* **1997**, *61*, 721–725.
5.　Rasmussen, B.; Fletcher, I.R. Zirconolite: A new U-Pb chronometer for mafic igneous rocks. *Geology* **2004** *32*, 785–788.
6.　Seddio, S.M.; Jolliff, B.L.; Korotev, R.L.; Zeigler, R.A. Petrology and geochemistry of lunar granite 12032, 366–19 and implications for lunar granite petrogenesis. *Am. Mineral.* **2013**, *98*, 1697–1713.
7.　Gieré, R; Williams C.T.; Lumpkin, G.R. Chemical characteristics of natural zirconolite. *Schweiz. Miner. Petrogr. Mitt.* **1998**, *78*, 433–459.
8.　Helean, K.B.; Navrotsky, A.; Vance, E.R.; Carter, B.; Ebbinghaus, B.; Krikorian, O.; Lian, J.; Wang, L.M.; Catalano, J.G. Enthalpies of formation of Ce-pyrochlore, $Ca_{0.93}Ce_{1.00}Ti_{2.035}O_{7.00}$, U-pyrochlore, $Ca_{1.46}U^{4+}_{0.23}U^{6+}_{0.46}Ti_{1.85}O_{7.00}$ and Gd-pyrochlore, $Gd_2Ti_2O_7$: Three materials relevant to the proposed waste form for excess weapons plutonium. *J. Nucl. Mater.* **2002**, *303*, 226–239.
9.　Gilligan, R.; Nikoloski, A.N. Leaching of brannerite in the ferric sulphate system. Part 1: Kinetics and reaction mechanism. *Hydrometallurgy* **2015**, *156*, 71–80.
10.　Gilligan, R.; Nikoloski, A.N. Leaching of brannerite in the ferric chloride system. *Hydrometallurgy* **2018**, *180*, 104–112.
11.　Nettleton, K.C.A.; Nikoloski, A.N.; Da Costa, M. The leaching of uranium from betafite. *Hydrometallurgy* **2015**, *157*, 270–279.
12.　Gilligan, R.; Nikoloski, A.N. Alkaline leaching of brannerite. Part 1: Kinetics, reaction mechanisms and mineralogical transformations. *Hydrometallurgy* **2017**, *169*, 399–410.
13.　Williams, C.T. The occurrence of niobian zirconolite, pyrochlore and baddeleyite in the Kovdor carbonatite complex, Kola Peninsula, Russia. *Mineral. Mag.* **1996**, *60*, 639–646.

14. Pöml, P.; Geisler, T.; Cobos-Sabaté, J; Wiss, T.; Raison, P.E.; Schmid-Beurmann, P.; Deschanels, X.; Jégou, C.; Heimink, J.; Putnis, A. The mechanism of the hydrothermal alteration of cerium- and plutonium-doped zirconolite. *J. Nucl. Mater.* **2011**, *410*, 10–23.

15. Bellatreccia, F.; Della Ventura, G.; Williams, C.T.; Lumpkin, G.R.; Smith, K.L.; Colella, M. Non-metamict zirconolite polytypes from the feldspathoid-bearing alkalisyenitic ejecta of the Vico volcanic complex (Latium, Italy). *Eur. J. Mineral.* **2002**, *14*, 809–820.

16. Bellatreccia, F.; Della Ventura, G.; Caprilli, E.; Williams, C.T.; Parodi, G.C. Crystal-chemistry of zirconolite and calzirtite from Jacupiranga, São Paulo (Brazil). *Mineral. Mag.* **1999**, *63*, 649–660.

17. White, T.J.; Segall, R.L.; Hutchison, J.L.; Barry, J.C. Polytypic behaviour of zirconolite. *Proc. R. Soc. Lond. A* **1984**, *392*, 343–358.

18. Reed, S.J.N. *Electron Microprobe Analysis and Scanning Electron Microscopy in Geology*. 2nd ed.; Cambridge University: Cambridge, UK, 2008.

19. Chang, L.L.; Howie, R.A.; Zussman, J. In *Rock-Forming Minerals: Volume 5. Non-Silicates*, Deer, W.A., Howie, R.A.; Zussman, J, Eds.; Longman: London, UK, 1975.

20. Wenk, H.R.; Bulakh, A.G. *Minerals, Their Constitution and Origin*, Cambridge University Press: Cambridge, UK, 2004.

21. Lumpkin, G.R.; Smith, K.L.; Blackford, M.G. Partitioning of uranium and rare earth elements in Synroc: Effect of impurities, metal additive, and waste loading. *J. Nucl. Mater.* **1995**, *224*, 31–42.

22. Gilligan, R.; Deditius, A.P.; Nikoloski, A.N. Leaching of brannerite in the ferric sulphate system. Part 2: Mineralogical transformations during leaching. *Hydrometallurgy* **2016**, *159*, 95–106.

23. Charalambous, F.A.; Ram, R.; Pownceby, M.I.; Tardio, J.; Bhargava, S.K. Chemical and microstructural characterisation studies on natural and heat treated brannerite samples. *Miner. Eng.* **2012**, *39*, 276–288.

24. McMaster, S.A.; Ram, R.; Pownceby, M.I.; Tardio, J.; Bhargava, S.K. Characterisation and leaching studies on the uranium mineral betafite [(U,Ca)$_2$(Nb,Ti,Ta)$_2$O$_7$]. *Miner. Eng.* **2015**, *81*, 58–70.

25. McMaster, S.A.; Ram, R.; Faris, N.; Pownceby, M.I.; Tardio, J.; Bhargava, S.K. Uranium leaching from synthetic betafite: [(Ca,U)$_2$(Ti,Nb,Ta)$_2$O$_7$]. *Int. J. Miner. Process.* **2017**, *160*, 58–67.

26. Strachan, D.M.; Scheele, R.D.; Icenhower, J.P.; Buck, E.C.; Kozelisky, A.E.; Sell, R.L.; Elovich, R.J.; Buchmiller, W.C. Radiation Damage Effects in Candidate Ceramics for Plutonium Immobilization; Final Report, PNNL-14588; Pacific Northwest National Laboratory: Richland, WA, USA, 2004.

27. Roinne, A. *SC Chemistry software*, version 7.1.1; Chemical Reaction and Equilibrium Modules. Outotec Research: Pori, Finland, 2012.

28. Gilligan, R.; Nikoloski, A.N. Alkaline leaching of brannerite. Part 2: Leaching of a high-carbonate refractory uranium ore. *Hydrometallurgy* **2017**, *173*, 224–231.

29. Knauss, K.G.; Dibley, M.J.; Bourcier, W.L.; Shaw, H.F. Ti(IV) hydrolysis constants derived from rutile solubility measurements made from 100 to 300 °C. *Appl. Geochem.* **2001**, *16*, 1115–1128.

30. Schmidt, J.; Vogelsberger, W. Aqueous Long-Term Solubility of Titania Nanoparticles and Titanium (IV) Hydrolysis in a Sodium Chloride System Studied by Adsorptive Stripping Voltammetry. *J. Solut. Chem.* **2009**, *38*, 1267–1282.

31. Thompson, J.V. Titanium pigments from Colorado perovskite. In Proceedings of the SME Annual Meeting, Salt Lake City, UT, USA, February 26–March 1 1990.

32. Gupta, C.K. *Chemical Metallurgy: Principles and Practice*. John Wiley & Sons: Weinheim, Germany, 2003.

33. Zhang, Y.; Hart, K.P.; Bourcier, W.L.; Day, R.A.; Colella, M.; Thomas, B.; Aly, Z.; Jostsons, A. Kinetics of uranium release from Synroc phases. *J. Nucl. Mater.* **2001**, *289*, 254–262.

34. Gilligan, R. The extractive metallurgy of brannerite: Leaching kinetics, reaction mechanisms and mineralogical transformations. Ph.D. thesis, Murdoch University, Perth, Australia, 2017.

35. Langmuir, D. *Aqueous Environmental Geochemistry*. Prentice Hall: Portland, ME, USA, 1997.

36. Pabst, A. The metamict state. *Am. Mineral.* **1952**, *37*, 137–157.

37. Ebbinghaus, B.B.; Armantrout, G.A.; Gray, L.; Herman, C.C.; Shaw, H.F.; Van Konynenburg, R.A. *Plutonium Immobilization Project Baseline Formulation*, Lawrence Livermore National Laboratory: Livermore, CA, USA, 2000; UCRL-ID-133089, rev. 1. PIP-00-141.